

Supplementary Material for Data Repository

MODEL DESIGN AND PARAMETER CHOICE

We model the development of large-hot orogens using a two-dimensional (2D) finite element code that assumes plane-strain conditions in a vertical cross-section through the orogen (e.g., Fullsack, 1995; Beaumont et al., 2004). The code computes thermal and mechanical evolution subject to velocity boundary conditions applied at the sides and base of the model region. Thermal-mechanical coupling occurs through the thermal activation of viscous power-law creep in the model materials and through the redistribution of radioactive crust by material flow.

We choose the simplest model design that is compatible with the first-order processes and features of natural orogenic systems - in this case, large, hot, collisional orogens with laterally variable lower crustal strength. The advantages and limitations of this approach are discussed by Beaumont et al. (2006). The model properties are similar to those described by Beaumont et al. (2004, 2006) and Jamieson et al. (2002, 2004). The model shown in Fig. DR1 is 2000 km wide, and has two regions - the crust, in which the velocity and deformation are calculated dynamically; and the mantle, where the velocity is prescribed kinematically. Model parameters and values are given in Table DR1.

Velocity boundary conditions and reference frame

Both the pro- and retro-mantle lithospheres (Fig. DR1) converge at a uniform velocity, $V_P = -V_R = 1.0$ cm/y (Model 1) and 2.5cm/y (Model 2) and detach and subduct beneath the stationary S-point (Willett et al., 1993). The subducted mantle lithosphere descends into the mantle with constant, kinematically specified, velocity. This frame of reference and associated symmetric convergence were chosen to give results that depend as little as possible on the motion of the lithospheric plates with respect to the sublithospheric mantle. The models can be interpreted in other reference frames (Beaumont et al., 2004) by adding or subtracting a fixed velocity to all of the boundary velocities and the velocity of the S-point. The change in reference frame does not change the model results, only the way in which they are viewed.

Model grid

The mechanical model used to calculate the velocity fields and deformation uses an Arbitrary Lagrangian Eulerian (ALE) methodology in which flows with free upper surfaces and large deformation are calculated on an Eulerian finite element grid that stretches in the vertical

direction to conform to the material domain (Fallsack, 1995). A Lagrangian grid, which is advected with the model velocity field, is used to update the mechanical and thermal material property distributions on the Eulerian grid as their position changes. Flow is driven by the basal and lateral velocity boundary conditions described above.

The Eulerian mechanical grid has 201 x 41 nodes (2000 x 35 km; crust only) and the thermal grid (crust and mantle) has 201 x 68 nodes (2000 x 96 km). The initial dimensions of the Lagrangian crustal grid are 5000 x 35 km (501 x 41 nodes). In the diagrams, deformation is displayed using a passive marker grid in which initial vertical markers are spaced at 40 km and horizontal markers at 5 km, with heavy vertical lines initially at 200 km intervals. The length of the timesteps, Δt , is 3000 y. Model times are quoted in My (millions of years after start of model).

Mechanical model and rheological parameters

The finite-element model uses a viscous-plastic rheology. The plastic (frictional or brittle) deformation is modelled with a pressure-dependent Drucker-Prager yield criterion. Yielding occurs when

$$(J_2')^{1/2} = P \sin \phi_{eff} + C \cos \phi_{eff} \quad (\text{DR1})$$

where J_2' is the second invariant of the deviatoric stress, P the dynamical pressure (mean stress), C the cohesion, and the internal angle of friction, ϕ_{eff} , is defined to include the effects of pore fluid pressures through the relation

$$P \sin \phi_{eff} = (P - P_f) \sin \phi. \quad (\text{DR2})$$

For dry frictional sliding conditions (approximating Byerlee's law), $\phi = 30^\circ$ when the pore fluid pressure, $P_f = 0$. For hydrostatic fluid pressures and typical crustal densities ϕ_{eff} is approximately 15° , and for overpressured pore fluid conditions we use $\phi_{eff} = 5^\circ$. Further details are given in Beaumont et al. (2006).

The flow is viscous when the flow stress is less than the plastic yield stress for the local ambient conditions. Under these circumstances the power law creep effective viscosity is

$$\eta_{eff}^V = B^* \cdot (J_2')^{(1-n)/2n} \cdot \exp[Q / nRT_K]. \quad (\text{DR3})$$

The values of B^* , n , and Q (Table DR1) are based on laboratory experiments with A values converted to B^* assuming cylindrical creep tests. In the present models, which were designed to investigate collision with progressively stronger lower crust, the mechanical properties of the

upper and middle crust are laterally uniform, while the strength of the lower crust is laterally variable. Model flow laws are based on a reference set of well constrained laboratory results - wet quartz (WQ) (melt-absent wet Black Hills quartzite; Gleason and Tullis, 1995) and dry diabase (DMD) (dry Maryland diabase; Mackwell et al., 1998). We have chosen to vary our model rheologies by scaling the parameters in these datasets in order to minimize the number of sources of error (e.g., resulting from variable experimental methods and starting materials) while allowing some variation in the model viscous flow properties.

Flow laws for model materials that are stronger or weaker than the reference set are constructed by linearly scaling up or down the values of B^* (Eq. DR3). This approach is used to approximate other material rheologies. The scaled viscosities can be interpreted in terms of the effects of composition and/or the consequences of water-saturated vs. water-poor (wet vs. dry) conditions. Alternatively they can be interpreted as synthetic model rheologies. Given that relative ductile flow of different materials in the models is mainly a consequence of their viscosity contrast, the simple scaling guarantees that the viscosity contrast is always given by the scaling factor under the same ambient conditions. The approach simplifies the interpretation of model results - instead of having results in which all of the parameters in the power-law creep flow law vary (Eq. DR3), only the effective viscosity varies as B^* is scaled. We believe that this scaling is an appropriate way to test the sensitivity of the models to the effect of wet vs. dry conditions or to a moderate change in composition. For example, $B^*(\text{DRY})$ is in the range $10\text{--}50 \times B^*(\text{WET})$, and $B^*(\text{WQ} \times 5)$ approximates conditions when flow is influenced by a mineral such as feldspar that has a higher effective viscosity than wet quartz for the ambient conditions.

In Models 1 and 2 (Figs 1 and 2, Table DR1), the rheology of the upper and middle crust is based on the 'Wet Black Hills Quartzite' (WQ) flow law (Gleason and Tullis, 1995). We use $B^* = B^*(\text{WQ})$ in the uppermost crust, which also has weak frictional-plastic properties, $\phi_{\text{eff}} = 5^\circ$. In Model 1 the mid-crust B^* is scaled by a factor of 5 ($B^* = B^*(\text{WQ} \times 5)$) and $\phi_{\text{eff}} = 15^\circ$. This layering is designed to approximate upper crust dominated by quartz-rich sedimentary rocks with high pore fluid pressures and middle crust comprising quartzo-feldspathic low- to medium-grade metasedimentary and granitic rocks.

The lateral variation in lower crustal strength in the models is intended to approximate collision involving a strong craton flanked by progressively less refractory crust (e.g. accreted terranes). Given uncertainties in the composition and other properties of the lower crust, we

argue that a reasonable approximation of power-law creep of the lower crust can be based on proxy materials ranging from $\eta_{eff} = B^*(DMD)$ (strong, dry, mafic granulite) to $\eta_{eff} = B^*(DMD/20)$ (weaker, partially hydrated, intermediate lower crust). The lateral strength variation is incorporated through a stepped reduction in effective viscosity from a maximum, $B^*(DMD)$, at the outer edge of the model to a minimum, $B^*(DMD)/20$, at the center. The model rheological structure is symmetric about the centre (Fig. DR1). Lower crustal blocks are initially 250 km wide and strength reductions occur in steps of $B^*(DMD)/4$. We choose dry Maryland diabase ($B^*(DMD)$) to represent the strongest lower crustal rheology, knowing that a comparison demonstrates that $B^*(DMD/10)$ corresponds closely to the power-law flow properties of intermediate Pikwitonei granulite (Wilks and Carter, 1990; Mackwell et al., 1998). We do not imply that the lower crust is diabase.

Melt weakening

The most important additional property is an extra increment of viscous weakening in the upper and middle crustal materials (those based on the WQ flow law) such that the effective viscosity decreases linearly with temperature from the dynamically determined power law creep value at $T = 700^\circ\text{C}$ to 10^{19} Pa.s at $T \geq 750^\circ\text{C}$. This weakening approximates the reduction in bulk viscosity caused by a small amount of *in situ* partial melt, estimated to be ca. 7% at the melt connectivity transition (Rosenberg and Handy, 2005). The melt weakening used in the present models amounts to approximately a factor of 10 decrease in effective viscosity, probably a conservative estimate for weakening by a small percentage of *in situ* melt. The lower crust in the models does not melt weaken because it is considered refractory and not prone to dehydration melting at the temperatures achieved in these models.

Model materials can therefore deform according to two mechanisms; plastic or viscous flow, and in the latter case the viscosity may be further reduced by melt weakening in quartz based materials. In all instances, the material deforms according to the mechanism that produces the lowest level of the second invariant of the deviatoric stress for the prevailing conditions; that is, the weakest of the available flow regimes is chosen.

Thermal model

The thermal evolution is calculated by solving the heat balance equation,

$$\rho C_p \partial T / \partial t + \underline{v} \cdot \nabla T = K \nabla^2 T + A \quad (\text{DR4})$$

on an Eulerian finite element mesh, where ρ is density, C_p is specific heat, T is temperature, t is time, \underline{v} is the advection velocity of the material, K is thermal conductivity, and A is radioactive heat production per unit volume. The Eulerian finite element mesh is the same as that for the mechanical model in the crust and continues into the underlying mantle. The advection velocities are calculated dynamically in the crust and are prescribed kinematically in the mantle.

The values of K , ρ (thermal density), and C_p are uniform throughout the model lithosphere, resulting in uniform thermal diffusivity, κ (Table DR1). The upper crust (0-20 km) has a uniform radioactive heat production, $A_1 = 2.0 \mu\text{W}/\text{m}^3$, and the lower crust (20-35 km) has lower heat production, $A_2 = 0.75 \mu\text{W}/\text{m}^3$ (Jamieson et al., 2002) (Table DR1).

Models are initialized with a steady-state temperature field, surface temperature of 0°C , basal heat flux, $q_m = 20 \text{ mW}/\text{m}^2$, and no heat flux through horizontal side boundaries. For these conditions and thermal conductivity $K = 2.00 \text{ W}/\text{m}^\circ\text{C}$, the initial surface heat flux $q_s = 71.25 \text{ mW}/\text{m}^2$, and the Moho temperature is 704°C .

Density structure and isostatic compensation

The model crust has a uniform density (Table DR1); no account is taken of density changes owing to variations in thermal expansion, melting, or metamorphism. This approach is adopted so that gravitational forces act equally on all materials and none of the crustal flow results from differential buoyancy forces caused by density variations. The changing crustal thickness is isostatically compensated by elastic flexure of a beam (flexural rigidity, $D = 10^{22} \text{ Pa}\cdot\text{s}$) embedded in the model at the base of the crust. Flexure only plays a minor role at the edges of the thickened crust. Elsewhere, broad regions of uniformly thick crust are effectively locally isostatically compensated.

Surface processes

In order to demonstrate the effects of surface processes one side of the symmetric models is subject to erosion. The local erosion rate is $\mathcal{E}(t,x) = \text{slope} \times f(t) \times g(x)$, where slope is the local surface slope determined from the Eulerian finite element mesh, $f(t)$ is a time function which is constant in the models used here, and $g(x)$ is a 'climate' function such that 0 represents an arid climate that does not lead to erosion and 1 represents a wet, highly erosive, climate. The combination of these variables produces a moderate erosion rate on the right-hand side of Model 1, with corresponding exhumation of proximal lower crustal nappes (Fig. DR1f); the equivalent model result in the absence of erosion is demonstrated on the left-hand side of the model (Fig.

DR1b-e). The region of Model 2 shown in Figure 2 had no syn-tectonic erosion. The upper crust has, however, been removed in the figure to approximate the effect of post-tectonic erosion, so that the model is comparable to the crustal cross sections shown above.

S-I Models 1 and 2

The S-I models exhibit a diachronous three-phase evolution during continuous convergence, leading to the development of ductile infrastructure decoupled from strong superstructure. During Phase 1, the crust progressively shortens and thickens by nearly uniform contraction (Fig. DR1c). Phase 2 involves thermal relaxation of thickened crust (Fig. DR1c) to produce hot, variably ductile middle and lower crust and relatively cool, strong, frictional-plastic upper crust. Phase 3 is the tectonic activation of ductile flow in response to underthrusting of a strong lower crustal indenter (Fig. DR1c,d). The incubation time is the time taken for Phases 1 and 2 to thicken and heat each vertical column of crust so that it is weak enough to be on the threshold of ductile flow, which can then be triggered by tectonic or gravitational forces (Beaumont et al., 2006). Incubation times and associated crustal thicknesses would be different for orogens with different thermal-mechanical properties (e.g., crust or mantle heat production, initial vertical or lateral strength profiles, convergence velocity) or geological histories (e.g. voluminous synconvergent plutonism).

The effects of varying a few key parameters are shown by the differences between Model 1 and Model 2. In Model 1, the upper and middle crustal layers are each 10 km thick at the start of the model, with the lower crust 15 km thick. In Model 2, the upper crustal layer initially extends from 0-10 km, the middle crustal layer extends from 10-25 km, and the lower crust extends from 25-35 km. The middle crust in Model 2 is weaker ($B^*(WQ \times 3)$) by comparison with Model 1 ($B^*(WQ \times 5)$), and the Model 2 convergence velocity is 2.5 cm/y instead of 1.0 cm/y. Thermal and other parameters are the same in both models. Despite the different initial crustal thickness and strength profiles and convergence velocities, both models develop ductile infrastructure that is decoupled from and injected beneath the superstructure. Because thermal properties are the same, the minimum incubation time in both cases is ca. 20 My. However, in Model 1 (slower convergence rate) collision with the indenter occurs at 60 My, and in Model 2 collision occurs at 25 My. The corresponding Phase 3 infrastructure develops from 70-100 My in Model 1 and 30-40 My in Model 2. These results demonstrate that similar S-I relationships can develop in models that evolve with quite different timescales and moderately different crustal properties.

References

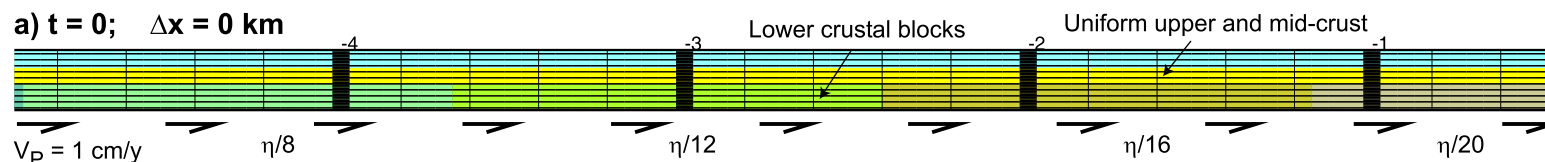
- Beaumont, C., Jamieson, R.A., Nguyen, M.H., and Medvedev, S., 2004, Crustal channel flows: 1. Numerical models with applications to the tectonics of the Himalayan-Tibetan orogen. *Journal of Geophysical Research*, v. 109, B06406 10.1029/2003 JB002809.
- Beaumont, C., Nguyen, M.H., Jamieson, R.A. & Ellis, S. 2006, Crustal flow modes in large hot orogens: In: Law, R.D., Searle, M.P. & Godin, L. (eds) *Channel flow, ductile extrusion, and exhumation of lower-mid crust in continental collision zones*. Geological Society, London, Special Publication, in press.
- Fullsack, P., 1995, An arbitrary Lagrangian-Eulerian formulation for creeping flows and its application in tectonic models: *Geophysical Journal International*, v. 120, p.1-23.
- Gleason, G.C., and Tullis, J., 1995, A flow law for dislocation creep of quartz aggregates determined with the molten salt cell: *Tectonophysics*, v. 247, p. 1-23.
- Jamieson, R.A., Beaumont, C., Nguyen, M.H., and Lee, B., 2002, Interaction of metamorphism, deformation, and exhumation in large convergent orogens: *Journal of Metamorphic Geology*, v. 20, p. 9-24.
- Jamieson, R.A., Beaumont, C., Medvedev, S., and Nguyen, M.H., 2004, Crustal channel flows: 2. Numerical models with implications for metamorphism in the Himalayan-Tibetan orogen: *Journal of Geophysical Research*, v. 109, B06406, doi:10.1029/2003JB002811.
- Mackwell, S.J., Zimmerman, M.E., and Kohlstedt, D.L., 1998, High-temperature deformation of dry diabase with application to tectonics on Venus: *Journal of Geophysical Research*, v. 103, p. 975-984.
- Rosenberg, C.L., and Handy, M.R., 2005, Experimental deformation of partially melted granite revisited: Implications for the continental crust: *Journal of Metamorphic Geology*, v. 23, p.19-28.
- Wilks, K.R., and Carter, N.L., 1990, Rheology of some continental crustal rocks: *Tectonophysics*, v. 182, p. 57-77.
- Willett, S., Beaumont, C., and Fullsack, P., 1993, A mechanical model for the tectonics of doubly-vergent compressional orogens: *Geology*, v. 21, p. 371-374.

Figure DR1: Results from Model 1, representing a convergent orogen with variable lower crustal strength. Model parameters and other details in Table DR1 and Supplement; additional results and animations available from <http://geodynamics.oceanography.dal.ca>. As described in Supplement, Model 1 is symmetric except for erosion (none on left side; moderate on right side).

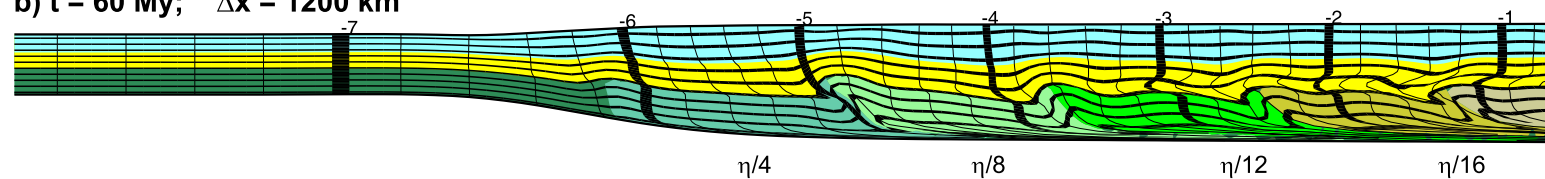
a) Initial conditions. Lower crustal blocks initially 15 km thick x 250 km wide; maximum effective viscosity (η = dry Maryland diabase, $B^*(DMD)$; Mackwell et al., 1998, dark green) successively reduced by factors of 4, 8, 12, 16, and 20, (lighter greens) from edge to centre of model. Upper (blue) and mid-crustal (yellow) layers are laterally uniform; mid-crust affected by melt-weakening at $T > 700^\circ\text{C}$ (Table DR1). b) Left and right sides after 60 My of Phase 1 convergence and Phase 2 heating. Contraction of upper crust (superstructure) produces upright, broadly symmetrical structures; in natural orogens thrust faults (not possible in this continuum mechanics model) should also be produced at this level. Asymmetric structure in lower crust reflects detachment from underlying mantle. Although incipient decoupling has developed between lower and upper crust in orogenic core, ductile flow in weak lower crust has not yet been activated. c) Activation of lower crustal flow by strong indenter (dark green) creates ductile infrastructure. Weak lower crustal blocks detach from mantle and develop tight asymmetric folds (proto-nappes). d) Continued convergence leads to expulsion of lower crustal nappes over indenter (box C is equivalent to Model 2 result shown in Fig. 2e). e) Right side shows effect of moderate erosion; lower crustal nappes are partially exhumed and young infrastructure (yellow, blue) is juxtaposed with old superstructure (green) in the vicinity of the orogenic front.

left side (No erosion)

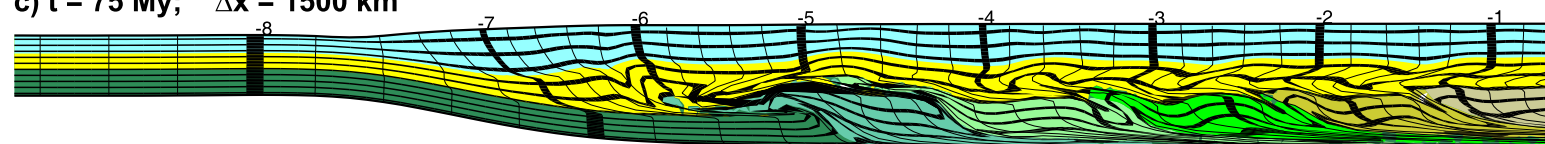
a) $t = 0$; $\Delta x = 0$ km



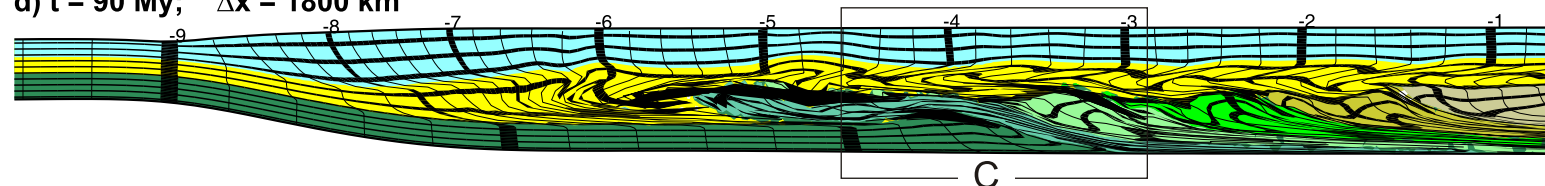
b) $t = 60$ My; $\Delta x = 1200$ km



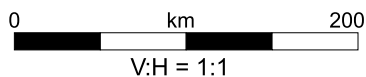
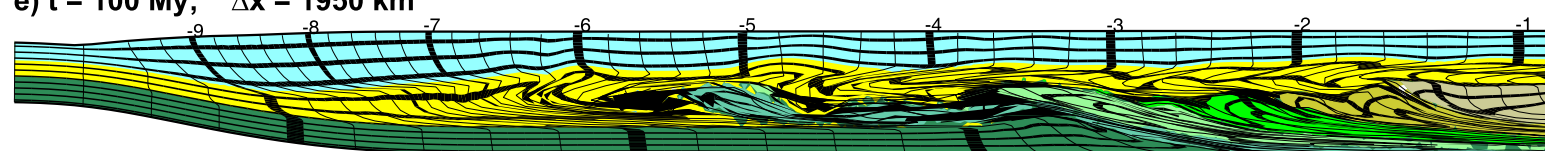
c) $t = 75$ My; $\Delta x = 1500$ km



d) $t = 90$ My; $\Delta x = 1800$ km



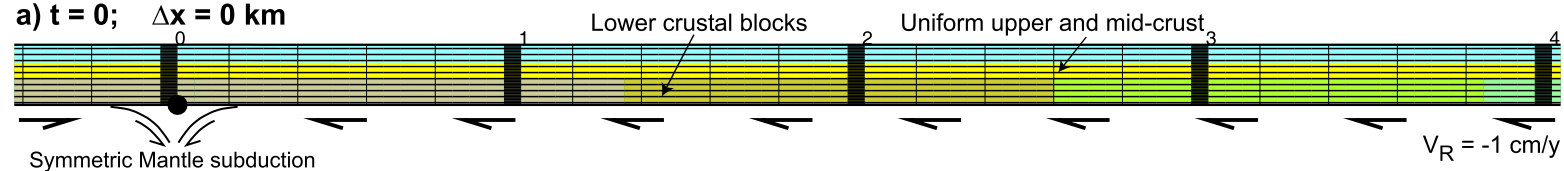
e) $t = 100$ My; $\Delta x = 1950$ km



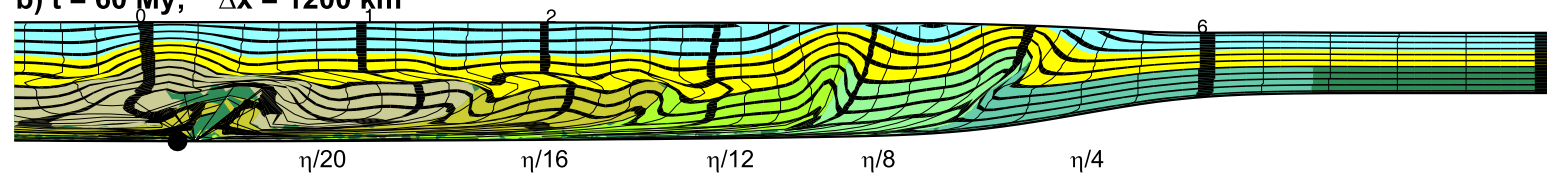
Culshaw et al.

right side (with erosion)

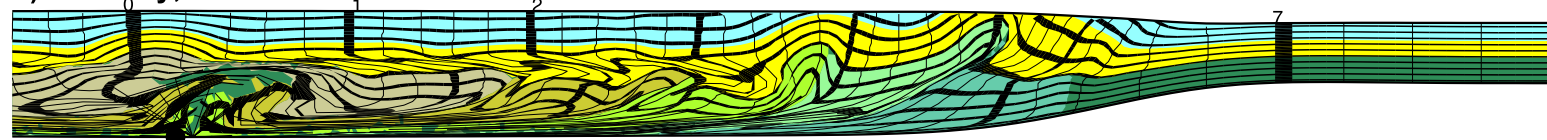
a) $t = 0$; $\Delta x = 0$ km



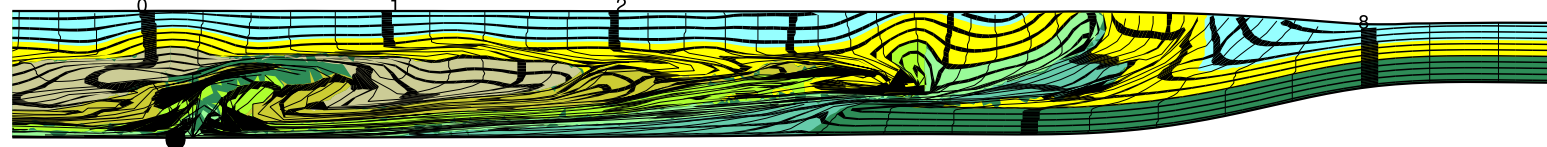
b) $t = 60$ My; $\Delta x = 1200$ km



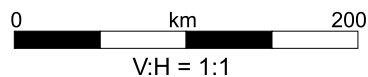
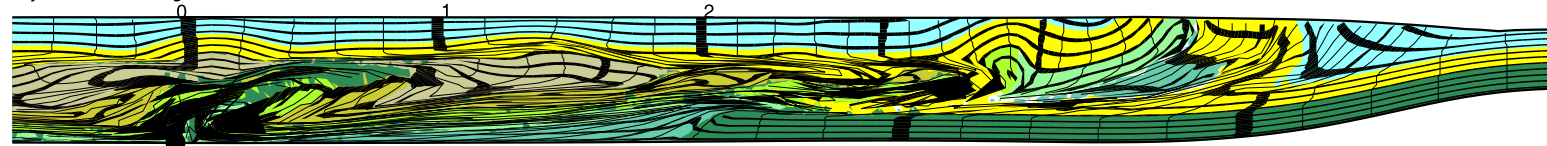
c) $t = 75$ My; $\Delta x = 1500$ km



d) $t = 90$ My; $\Delta x = 1800$ km



e) $t = 100$ My; $\Delta x = 1950$ km



Culshaw et al.

Data Repository Table 1. Parameters used in models (Fig. 1, 2, DR1). Details of model design, choice of parameters, and implementation can be found in Fulsack (1995), Beaumont et al. (2004), and Beaumont et al. (2006), and accompanying Supplement.

Parameter	Meaning	Value(s)
a) Mechanical parameters for Model 1 (Fig. 1)		
ρ_{crust}	crustal density	2700 kg/m ³
ρ_{mantle}	mantle density	3300 kg/m ³
D	flexural rigidity in isostasy model	10 ²² Nm
	crustal thickness	35 km
	lower crustal thickness	15 km
	width of Eulerian model domain	2000 km
ϕ_{eff} (0 – 10 km)	effective internal angle of friction (upper crust)	5°
ϕ_{eff} (10 – 35 km)	effective internal angle of friction (mid- and lower crust)	15°
C	cohesion	10 MPa
P	solid pressure	Pa
P_f	pore fluid pressure	Pa
J_2'	second invariant of the deviatoric stress tensor	Pa ²
$\eta_{eff}^v = B * (\dot{I}_2')^{(1-n)/2n} \exp[Q/nRT_K]$	general equation for effective viscosity	
\dot{I}_2'	second invariant of strain rate tensor	s ⁻²
R	gas constant	8.314 J/mol°K
T_K	absolute temperature	°K
B^*, n, Q as below		
WQ (0 – 10 km)	wet Black Hills quartzite flow law (after Gleason and Tullis, 1995)	$n = 4.0$ $B^* = 2.92 \times 10^6 \text{ Pa.s}^{1/4}$ $Q = 223 \text{ kJ/mol}$
WQ x 5 (10 – 20 km)	modified wet Black Hills quartzite flow law (as above except scaled by 5)	$B^* = B^* (\text{WQ}) \times 5$
DMD (20 – 35 km)	dry Maryland diabase flow law (after Mackwell et al., 1998)	$n = 4.7$ $B^* = 1.91 \times 10^5 \text{ Pa.s}^{1/4.7}$ $Q = 485 \text{ kJ/mol}$
DMD flow law scaled by weakening factor, w		
DWD/w where w = 4, 8, 12, 16, 20		
DMD/w	modified dry Maryland diabase flow law	$B^* = B^* (\text{DMD})/w$
'melt weakening'	linear reduction in effective viscosity over T range 700-750°C for WQ and WQ x 5 only	η_{700} = flow law value $\eta_{750} = 10^{19} \text{ Pa.s}$

DR Table 1 (continued):

b) Mechanical parameters for Model 2 (Fig. 2); as for Model 1 except:

WQ x 3 (10 – 25 km)	lower crustal thickness	10 km
	modified wet Black Hills quartzite	$B^* = B^* (\text{WQ}) \times 3$
	flow law (as above except scaled by 3)	
DMD (25 – 35 km)	dry Maryland diabase flow law	$n = 4.7$
	[after <i>Mackwell et al.</i> , 1998]	$B^* = 1.91 \times 10^5 \text{ Pa.s}^{1/4.7}$
		$Q = 485 \text{ kJ/mol}$
DMD flow law scaled by weakening factor, w		
DWD/w where w = 8, 12, 16, 20		
DMD/w	modified dry Maryland diabase flow law	$B^* = B^* (\text{DMD}) / w$
'melt weakening'	linear reduction in effective viscosity	$\eta_{700} = \text{flow law value}$
	over T range 700-750°C	$\eta_{750} = 10^{19} \text{ Pa.s}$
	for WQ and WQ x 3 only	

c) Basal velocity boundary conditions for Model 1:

V_P	left-side (convergence) velocity	1 cm/y
V_R	right-side velocity	-1 cm/y
V_S	S-point velocity	0 cm/y

d) Basal velocity boundary conditions for Model 2:

V_P	left-side (convergence) velocity	2.5 cm/y
V_R	right-side velocity	-2.5 cm/y
V_S	S-point velocity	0 cm/y

e) Thermal parameters for Models 1 and 2:

K	thermal conductivity	2.00 W/m°K
κ	thermal diffusivity	$1.0 \times 10^{-6} \text{ m}^2/\text{s}$
	($\kappa = K / \rho C_p$, where $\rho C_p = 2 \times 10^6$)	
T_s	surface temperature	0°C
T_a	temperature at lithosphere/ asthenosphere boundary	1350°C
q_m	basal mantle heat flux	20 mW/m ²
q_s	initial surface heat flux	71.25 mW/m ²
A_1 (0-20 km)	upper crustal heat production	$2.0 \times 10^{-6} \text{ W/m}^3$
A_2 (20-35 km)	lower crustal heat production	$0.75 \times 10^{-6} \text{ W/m}^3$

DR Table 1 (continued):

f) Surface denudation for Model 1 (right-side only, Fig. 1)

slope $\times f(t) \times g(x)$	denudation rate (m/y)	
slope	local surface slope (measured from finite element mesh)	
$f(t)$	time function (0 – 100 My)	
	specifies how denudation rate (m/y) varies with time when $g(x)$ and slope = 1	
$g(x)$	spatial function	
	specifies how denudation rate varies with position x	
	$g(x) = 0$ = arid	
	$g(x) = 1$ = wet	
$f(t)$	0.027 m/y	$t > 0$ (ie constant)
$g(x)$	0.0	$0 < x \leq 1450$ km
	varies linearly 0.0 \rightarrow 1.0	$1450 < x < 1500$ km
	1.0	$x \geq 1500$ km

g) Surface denudation for Model 2; as for Model 1 except result shown in Fig. 2 is after post-orogenic denudation for comparison with observed seismic section

References (DR Table 1):

- Beaumont, C., Jamieson, R.A., Nguyen, M.H. and Medvedev, S. 2004. Crustal channel flows: 1. Numerical models with applications to the tectonics of the Himalayan-Tibetan orogen. *Journal of Geophysical Research* **109**, B06406, doi:10.1029/2003JB002809.
- Beaumont, C., Nguyen, M.H., Jamieson, R.A. and Ellis, S., 2006. Crustal flow modes in large hot orogens. *Geological Society of London Special Volume, Channel Flows*
- Fullsack, P., 1995. An arbitrary Lagrangian-Eulerian formulation for creeping flows and its application in tectonic models. *Geophysical Journal International*, **120**, 1-23.
- Gleason, G.C. and Tullis, J. 1995. A flow law for dislocation creep of quartz aggregates determined with the molten salt cell. *Tectonophysics*, **247**, 1-23.
- Mackwell, S.J., Zimmerman, M.E. and Kohlstedt, D.L. 1998. High-temperature deformation of dry diabase with application to tectonics on Venus. *Journal of Geophysical Research*, **103**, 975-984.